ICE FOG IN ARCTIC DURING FRAM–ICE FOG PROJECT

Aviation and Nowcasting Applications

BY I. GULTEPE, T. KUHN, M. PAVOLONIS, C. CALVERT, J. GURKA, A. J. HEYMSFIELD,
P. S. K. LIU, B. ZHOU, R. WARE, B. FERRIER, J. MILBRANDT, AND B. BERNSTEIN

Increased understanding of ice fog microphysics can improve frost and ice fog prediction using forecast models and remote-sensing retrievals, thereby reducing potential hazards to aviation.

Ice fog occurs usually at temperatures less than –15°C because of direct deposition of water vapor into ice nuclei. It significantly affects aviation and transportation in northern latitudes because ice fog causes low visibilities and ice crystal accumulation on the surface of structures. Ice fog may also be called frost fog consisting of ice crystals, formed under conditions of clear skies, very low temperatures, and little or no wind (Kumar 2004; National Snow and Ice Data Center Arctic Climatology and Meteorology Dictionary at http://nsidc.org/arcticmet/glossary/frost_point.html). The meteorological community defines ice fog as an event consisting of individual ice crystals that occur at temperatures usually less than –30°C. According to the American Meteorological Society (AMS) *Glossary of Meteorology* (Glickman 2000), ice fog is composed of suspended ice crystals with sizes of 20–100 μm in diameter and it occurs rarely at temperatures greater than –30°C. This definition uses a forecaster's point of view on visibility. Freezing fog is defined by the *Glossary of Meteorology* as consisting of droplets, which freeze upon contact with exposed objects and form a coating of rime and/or glaze (Petterssen 1940; Schaefer and Day 1981). Hoarfrost or frost forms a deposit of interlocking ice crystals (hoar crystals) formed by direct deposition on objects freely exposed to the air, such as tree branches, plant stems and leaf edges, wires, poles, etc. These definitions are considered in the course of this work.

Ice fog forecasting is usually very difficult (Gultepe et al. 2009, 2012) because of limited surface in situ and remote sensing observations, limited understanding of ice microphysics, and anthropogenic effects on ice crystal nucleation processes. The definition of ice

AFFILIATIONS: GULTEPE AND LIU—Cloud Physics and Severe Weather Research Section, Environment Canada, Toronto, Ontario, Canada; KUHN—Luleå University of Technology, Division of Space Technology, Kiruna, Sweden; PAVOLONIS—NOAA/NESDIS, Madison, Wisconsin; CALVERT—CIMSS, University of Wisconsin–Madison, Madison, Wisconsin; GURKA—NOAA/NESDIS, Greenbelt, Maryland; HEYMSFIELD—NCAR, Boulder, Colorado; ZHOU AND FERRIER—I.M. Systems Group, and NOAA/NWS/NCEP, Camp Springs, Maryland; WARE—Radiometrics Corporation, and CIRES, University of Colorado, Boulder, Colorado; MILBRANDT—RPN, CMC, Environment Canada, Dorval, Quebec, Canada; BERNSTEIN—Leading Edge Atmospherics, Boulder, Colorado
CORRESPONDING AUTHOR: Dr. Ismail Gultepe, Environment Canada, Cloud Physics and Severe Weather Research Section, 4905 Dufferin St., Toronto, ON M3H5T4, Canada
E-mail: ismail.gultepe@ec.gc.ca

The abstract for this article can be found in this issue, following the table of contents.
DOI:10.1175/BAMS-D-11-00071.1

In final form 21 July 2013

fog is given differently in various references, which further complicates its analysis. In this work, ice fog categories are defined as heavy ice fog for visibility <1 km (to be consistent with warm fog definitions), intermediate ice fog for visibility between 1 and 5 km, and light ice fog for visibility >5 km.

Ice fog may occur because of various mechanisms. Wexler (1936, 1941) explained how ice fog and light snow form when surface infrared radiative cooling occurs. His work suggested that strong radiative cooling at the surface was limited by the higher temperatures above the inversion layer. Radiative cooling at low levels propagates upward, during which a strong surface inversion forms but decreases in strength with time. At higher levels, an isothermal layer soon forms and its thickness increases with time. As a result, the inversion top decreases with subsidence, resulting in a weak upper inversion. Wexler (1936, 1941) suggested that ice fog and light snow, which usually occur in these conditions, were not recorded by sensors, resulting in an inaccurate estimate of the Arctic heat and water budgets. Bowling et al. (1968) suggested that ice fog events may occur in Alaska due to advection of a cold dome from Siberia, resulting in an anticyclonic circulation, and subsidence that warms the air above the initial cold dome. These studies suggest that ice fog events can be related to regional and larger-scale meteorological processes.

Earlier studies were limited in their understanding of microphysics of ice fog and light snow conditions (defined as precipitation rate <0.5 mm h^{-1}) because of measurement difficulties (Thuman and Robinson 1954; Robinson et al. 1957; Benson 1965; Benson and Rogers 1965; Ohtake 1967). Later, Wendler (1969) described the ice fog as a dense cirrostratus cloud near the surface. Gotaas and Benson (1965) studied two extreme ice fog events and suggested that cooling at the surface cannot only be related to cold air advection or heat loss from the air and snow surface. The temperature was less than –40°C for two cases (~9 and 6 consecutive days) during winter of 1961/62. They proposed that heat was radiated away from ice crystals, creating a strong temperature gradient in the vicinity of the ice crystals. Furthermore, relative humidity with respect to ice (RH_i) was less than saturation values during the occurrences of ice fog and light snow. For these events, the air in contact with crystals had lower temperature and was saturated with respect to ice. In their work, ice fog is primarily defined as a man-made phenomenon.

The size of ice fog particles is usually less than 200 μm and their fall speed is similar to fog droplets (Koenig 1971). Assuming that ice crystals form directly from vapor depositing onto ice nuclei, their growth can be different than those of large ice crystals. The understanding of ice fog formation was greatly improved by Koenig (1971) when he proposed a method to calculate ice crystal growth rates from depositional nucleation processes. He stated that diffusional growth of small ice crystals was much larger than ventilation effects, suggesting that ice fog particles grew likely because of vapor diffusion and as a strong function of crystal particle shape. Szyrmer and Zawadzki (1997) stated that ice forming nuclei issues remain an area of debate and the great majority of ice nuclei consist of soil mineral particles. Vapor deposition directly onto ice nuclei is the major source for ice fog particles, formation and growth. Although both ice nuclei composition and concentration play an important role for ice initiation (Zelenyuk and Imre 2005), they cannot be predicted or measured accurately (Gultepe and Isaac 2002; Szyrmer and Zawadzki 1997).

Many airborne sensors cannot measure ice fog particles with sizes less than 200 μm accurately because of the issues of shattering and sensor optical sensitivity in high speed environments (Gultepe et al. 2001; Lawson 2011; Lawson et al. 2006a,b; Field et al. 2006; Korolev et al. 2011). New sensors such as the two-dimensional stereographic probe (Lawson et al. 2010) are being used for small ice crystal detections in both flight conditions and at the surface (Lawson et al. 2010; Lawson 2011). Lawson et al. (2006a) made a detailed study of ice crystals using various in situ instruments including a cloud particle imaging probe and polar nephelometer at the South Pole Station; ice crystal number concentration of up to 500 L^{-1} was found for sizes <200 μm, suggesting that small ice crystals were abundant. Citing the work of Kumai (1964), Hobbs (1965) reported that a majority of ice fog particles were spherical and 74% of ice particles collected consisted of aggregates of two or more spherical particles at temperatures <–37°C. Similar work by Korolev and Isaac (2003) also stated that, using the cloud particle imaging measurements, ice crystals with sizes less than about 100 μm were spherical. Overall, these works suggested that the shapes of ice particles were mostly spherical for sizes less than 100 μm. Using ice crystal images and particle spectra, the results of the current project will shed a light on this issue.

Detailed studies of ice fog and light snow using the Northern Aerosol Regional Climate Model by Girard and Blanchet (2001) suggested that ice fog and diamond dust (defined as light snow) can significantly affect the radiative budget in the Arctic. Furthermore, they pointed out that ice fog and diamond dust may occur up to 30%–40% of time in the Arctic winter (Curry et al. 1990) and their radiative effect can be as high as 60 W m^{-2}. Their work suggested that both ice fog and diamond dust should be included in the model simulations.

The above studies suggested that measurement issues related to ice fog still exist and this complicates the development and validation of the ice fog microphysical parameterizations and its prediction using numerical forecasting models as well as the retrievals of ice fog microphysical properties from remote sensing platforms. In the present work, all the cases were used to represent ice fog conditions because temperature during the project was usually at least –15°C or colder and relative humidity with respect to water (RH_w) never reached 100% saturation with respect to water. Only one freezing fog case occurred during the project and is not considered in this study.

PROJECT OBJECTIVES. During the two months of the Fog Remote Sensing and Modeling–Ice Fog (FRAM-IF) project, horizontal visibility limitations of 0 to 10 km due to ice fog occurred 14 times over the Yellowknife International Airport, Northwest Territories (NWT), Canada. For this study, we have extended the visibility range associated with identifying fog to distances beyond the standard 1 km as emphasized in the introduction. Visibility due to ice fog was usually much lower in the town of Yellowknife compared to the project site at the airport, which is located at 6 km northwest of town center. This was because of anthropogenic aerosol contributions from heating systems and automobiles (see Fig. 1a).

The Arctic environment is very sensitive to small changes of moisture and temperature, leading to ice fog and light snow conditions. Gultepe et al. (2012) showed that accidents related to weather and low visibility conditions over the Arctic regions could increase tenfold in the near future because of increasing air traffic. This suggests that ice fog conditions can have major impacts on aviation and transportation, and also on climate. The FRAM-IF project goals are to develop better understanding of ice fog processes, its prediction using forecast models and remote sensing techniques, and its effects on aviation and local weather. These goals are summarized below:

1) Improve the understanding of the physical processes leading to ice fog formation.
2) Improve the understanding of the relationship between ice fog, frost, and light snow.
3) Develop an instrument suite for ice fog study.
4) Improve the understanding of the effects of ice fog and frost on aviation, transportation, and local weather.
5) Develop the skills for ice fog nowcasting using remote sensing, surface observations, and forecast models.
6) Discuss the effects of small ice crystals on the cloud microphysical processes and model simulations.

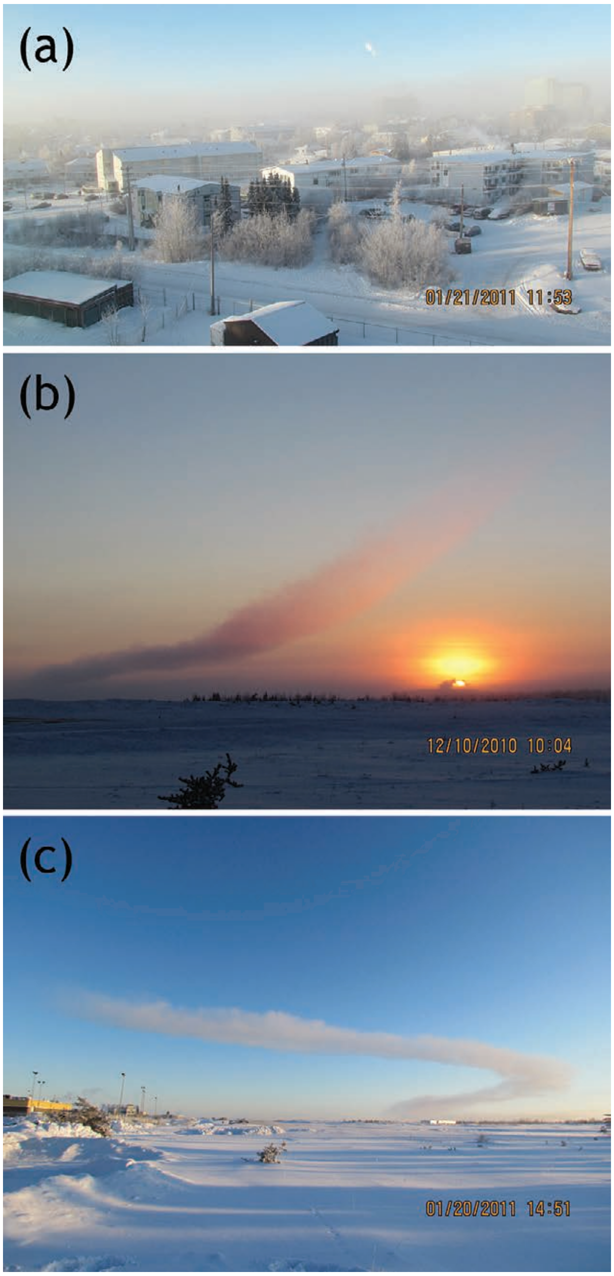

Fig. 1. (a) Ice fog event on 21 Jan 2011 over Yellowknife, NWT, Canada; (b) contrail remaining after an aircraft takes off at 1004 local standard time (LST) 10 Dec 2010; and (c) another contrail at 1451 LST 20 Jan 2011.

TABLE 1. Instruments deployed during the FRAM-IF fog project that took place over Yellowknife International Airport, NWT, Canada. The location given in first column is for the instrument location at the project site (see Fig. 2), Tr represents the trailer location, RH_w is the relative humidity with respect to water, and T is the temperature.

Instruments (with location number)	Definition	Measurement	Characteristics
(7) FMD (Droplet measurements Technologies, Inc.)	Fog monitoring device	Droplet spectra	1–50-μm size range
(1) GCIP (Droplet Measurements Technologies, Inc.)	Ground imaging probe	Droplet/ice spectra	15–930-μm size range
(7) OTT ParSiVel (Metek, Inc.)	Parsivel size velocity distrometer	Precipitation spectra	400 μm max size range
(2) CAP (Climatronics, Inc.)	Climatronics aerosol profiler	Droplet and aerosol spectra	0.3–10 μm; 8 channels
(6) T-200B (GEONOR, Inc.)	Precipitation sensor	Precipitation amount	Lower threshold 0.5 mm h^{-1}
(4) IPC (York University)	Ice particle counter	Ice particle spectra	15–500 μm
(6) FD12P (Vaisala, Inc.)	All weather precipitation sensor	Precipitation type and amount, and visibility	0.05 mm h^{-1}; lower threshold
(6) Sentry visibility (Envirotech, Inc.)	Sentry visibility sensor	Visibility	>10-m lower threshold
(5) CL31 (Vaisala, Inc.)	Ceilometer	Ceiling height	>10-m uncertainty
(2) TPS (Yankee Environmental Systems, Inc.)	Total precipitation sensor	Total precipitation rate and amount	>0.25 mm h^{-1} lower threshold
(2) DSC111 (Vaisala, Inc.)	Surface state condition sensor	Surface type and condition	—
(2) DST111 (Vaisala, Inc.)	Surface state temperature sensor	Surface temperature	—
(2) SR50 (Campbell Scientific, Inc.)	Sonic Ranger for snow depth	Snow depth	10%–20% uncertainty
(4) SW/IR radiometers (Eppley, Inc.)	Shortwave/infrared radiometers	Shortwave (SW) and IR broadband fluxes	10%–15% uncertainty
(2) UW 3D sensor (Young, Inc.)	Ultra Wind three-dimensional sensor	3D wind speed and direction, turbulence	4–32-Hz sampling rate
(4) Young wind sensor (Young, Inc.)	Two-dimensional wind sensor	2D wind speed and direction	1-min sampling rate
(2) SPN1 (AT Delta, Inc.)	Sunshine pyranometer	Direct; diffuse SW radiation	0.4–2.7 μm
(6) MRR (Biral, Inc.)	Microwave rain radar	Precipitation reflectivity and Doppler velocity	—
(7) MP-3000 MWR (Radiometrics Corporation)	Profiling microwave radiometer	Liquid water content, temperature, humidity, and RH_w profile	Liquid water content threshold > 0.1 g m^{-3}
(Tr) Microscope (Barska)	—	Ice crystal pictures	—
(2) RID 872E3 (Campbell Scientific, Inc.)	Rosemount icing detector	Icing rate	Liquid detection: 10%
(Tr) UHSAS (Droplet Measurements Technologies, Inc.)	Ultra high sensitivity aerosol spectrometer	Aerosol spectra	0.050–1-μm size range
(2) Pressure sensor (Vaisala, Inc.)	—	Pressure	1% uncertainty
(2) WXT520 (Vaisala, Inc.)	Present weather sensor	T, RH_w, wind speed and direction, rain, pressure	10% uncertainty
(4) CNR1 (Kipp & Zonen, Inc.)	Net radiometer	SW and IR up and down radiative fluxes	Pyranometer: 0.305–2.8 μm Pyrgeometer: 4.5–42 μm
(6) SWS-200 (Biral, Inc.)	Present weather sensor	Precipitation and visibility	10% uncertainty
(7) LPM 5.4110 (Biral, Inc.)	Laser precipitation monitor	Precipitation spectra	0.13–8 mm; 22 channels
(4) HMP45 (Campbell Scientific, Inc.)	Temperature and humidity probe	T and RH_w	Uncertainty: 1°C for T and 10% for RH_w

PROJECT SITE AND OBSERVATIONS. The FRAM-IF field project took place near the Yellowknife International Airport (62°27′46″N, 114°26′25″W), Yellowknife, NWT, Canada, between 25 November 2010 and 5 February 2011. The project site was at the northern section of the airport, away from takeoffs and landings. Flight paths were usually in the east–west direction. Figure 1a shows an ice fog event on 21 January 2011. Figures 1b and 1c show the formation of ice clouds (contrails) after aircraft takeoff from the Yellowknife International Airport on 10 December 2010 and on 20 January 2011, respectively. For both cases, the surface temperature was about –30°C. On several occasions, precipitating particles were observed after aircraft taking off, suggesting that ice crystals grew to larger sizes. Figure 2 shows the instruments deployed at the site. The instrument names, location at the project site, and measurements are listed in Table 1. These instruments were selected to obtain visibility, snow rate and accumulation amount, solar and infrared broadband fluxes, three-dimensional wind components at 1- and 16-Hz sampling rates, snow reflectivity, vertical temperature profile, vapor mixing ratio, and liquid water content.

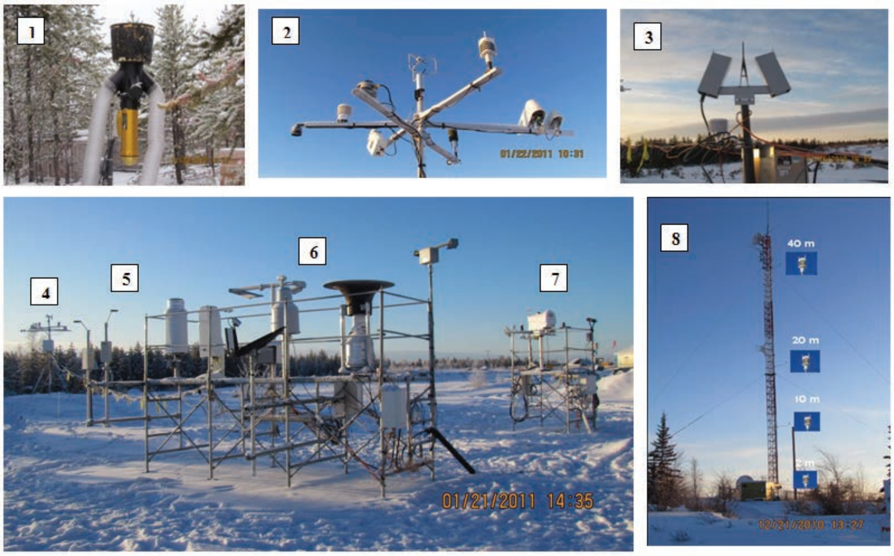

Fig. 2. Instruments deployed at the Yellowknife International Airport, NWT, Canada. The numbers shown represent the sensors or towers given in Table 1. The Jack Fish Tower (8) is used for obtaining meteorological parameters (temperature, relative humidity with respect to water, wind speed and direction, precipitation rate, pressure) over 1-min intervals from WXT520s mounted at 2-, 10-, 20-, and 40-m levels.

During the 2010/11 winter, mean hourly temperature values were significantly below the 47- and 10-yr averages of minimum temperature (1953–2000 and 2000–10, correspondingly). The RH_w value for 2010/11 was also lower than for other time periods. The cold high pressure systems with clear skies were one of the main reasons for ice fog and frost formation during the

Table 1. Continued.

Instruments (with location number)	Definition	Measurement	Characteristics
(4) HMP45C212 (Campbell Scientific, Inc.)	Temperature and humidity probe	T and RH_w	Uncertainty: 1°C for T and 10% for RH_w
(7) MP100A (Rotronic, Inc.)	Temperature and humidity probe	T and RH_w	Uncertainty: 1°C for T and 10% for RH_w
(Tr) ICI (Luleå Technical University)	Ice crystal imager	Ice crystal spectra	>100 μm detection threshold
(7) IceMeister-9734 (New Avionics, Inc.)	Icing sensor	Icing condition	5% uncertainty
(Tr) IR (DX501)/IRtC.20A-oE (Exergen, Inc.)	Infrared temperature sensor	Ceiling temperature	5% uncertainty
(4) POSS (Environment Canada)	Precipitation occurrence sensing system	Precipitation type and spectra	>500 μm for detection limit
(Tr) Axis camera system (AXIS Communications, Inc.)	IP camera system	Pictures	—

FRAM-IF project. In some cases, clear skies or radiative cooling were not sufficient for ice fog formation, probably because of the lack of ice nuclei and moisture.

During the project, particle spectra or shapes were measured by the Climatronic Aerosol Profiler, Ultra-High Sensitivity Aerosol Spectrometer, Fog Measuring Device Ground Cloud Imaging Probe, Laser Precipitation Monitor, Parsivel disdrometer, and Precipitation Occurrence Sensor System (Table 1). Ice crystals were imaged by a microscope, a Canon camera with macro capability, Ice Crystal Imaging probe, and Ground Cloud Imaging Probe (label 1 in Fig. 2) that was adapted from an aircraft instrument called the Droplet Measurement Technologies Cloud Imaging Probe. The Ground Cloud Imaging Probe measures fog and light precipitation properties. The small ice crystal size distributions of fog and snow particles over Ground Cloud Imaging Probe's 62 channels were obtained at 1-s intervals. The resolution of the spectra is 15 μm, and minimum and maximum sizes are about 7.5 and 930 μm, respectively. The smallest image obtained represents particles less than about 10 μm but its shape cannot be verified. The three main visibility sensors used during the project were the Vaisala FD12P, Sentry visibility sensor, and Metek SWS-200.

The Laser Precipitation Monitor (Table 1 and label 7 in Fig. 2) uses a parallel laser-light beam (0.780 μm, not visible) to detect the ice crystals and snow particles (also for droplets). A photodiode with a lens is situated on the receiver side in order to measure the light intensity by transforming it into an electrical signal. When a precipitation particle falls through the light beam over the measuring area of 45.6 cm^2 [sampling volume: 20 mm (width), 228 mm (length), and 0.75 mm (depth)], the receiving signal is reduced. The diameter of the particle is calculated from the duration of the reduced signal. The measured values are processed by a signal processor and then the intensity, quantity, and type of precipitation and the spectra are calculated.

The four WXT520s from Vaisala, Inc., were mounted along a 40-m tower (called Jack Fish Tower) at levels of 2, 10, 20, and 40 m (label 8 in Fig. 2) to obtain temperature and RH$_w$ profiles within the boundary layer. Each WXT520 provided temperature, RH$_w$, two-dimensional wind speed, direction, and precipitation type. These measurements will be used to validate microwave radiometer-based and model-based profiles at low levels (<40 m).

The ice crystal imaging sensor from the Luleå University of Technology is designed to sample ice and snow particles. Main components of ice crystal imaging sensor are inlet and microscope systems. The microscope imaging system is mounted underneath the sampling inlet that includes a funnel tapering system with a 25-mm (inner diameter) tube. This 25-mm tube is connected to an 8-mm nozzle and a 12-mm tube. The 12-mm tube is a co-centric sampling tube below the nozzle that acts as a virtual impactor. A flow of about 11 L min^{-1} is pumped through the nozzle of which only 3 L min^{-1} continues through the sampling tube to the imaging system, while the rest is pumped away from the space between the nozzle and sampling tube entrance. A laser beam traverses the sampling volume in a direction orthogonal to the axis of this imaging setup and is used to detect particles and trigger the imaging system. The pixel resolution is given by the choice of microscope objective and tube lens; in this setup, it is 4.2 μm per pixel so that particles between 20 μm and 2 mm can be imaged, and their size and shape can be determined. The charge-coupled device camera is interfaced to a laboratory computer that recorded the images.

An example of the profiling microwave radiometer retrieved temperature, RH$_i$, and vapor mixing ratio are shown in Figs. 3a–c, respectively. Figure 3b shows that the RH$_i$ in excess of 100% was observed below 3-km level where temperature (Fig. 3a) was between –20° and –35°C. Ice fog was observed below about 700 mb where vapor mixing ratio (Fig. 3c) reached up to 0.8 g kg^{-1}.

GOES-R APPROACH TO FOG/LOW CLOUD MONITORING.

FRAM-IF measurements will be used to validate and characterize satellite-based retrievals of fog and low cloud products developed for the next-generation series of Geostationary Operational Environmental Satellites (GOES-R), which is scheduled for launch in 2015. The Advanced Baseline Imager on GOES-R will offer more spectral bands, higher spatial resolution, and faster imaging than the current GOES Imager (Schmit et al. 2005, 2008). The Advanced Baseline Imager has 16 spectral bands compared to 5 on the current series of GOES Imagers (Schmit et al. 2001; Menzel and Purdom 1994). Algorithms have been developed for the Advanced Baseline Imager bands for characterizing cloud properties such as cloud phase and cloud base height (e.g., Pavolonis 2010a,b; Calvert and Pavolonis 2011).

Cloud phase determination.

The Advanced Baseline Imager cloud phase algorithm utilizes a series of infrared-based spectral and spatial tests to determine cloud phase (liquid water, supercooled water, mixed phase, ice). In lieu of the brightness temperature differences, effective absorption optical depth ratios are used in the spectral tests. As shown in Pavolonis

(2010a), effective absorption optical depth ratios allow for improved sensitivity to cloud microphysics, especially for optically thin clouds. Using the Moderate Resolution Imaging Spectroradiometer (MODIS), the GOES-R series cloud phase algorithm was tested during the FRAM-IF. Figures 4a and 4b show the false color image and cloud phase at a nighttime overpass of *Aqua* MODIS on 18 December 2010, indicating the presence of mixed phase and ice clouds at the vicinity of Yellowknife, which is consistent with surface observations. Figures 4c and 4d are for visibility and they are explained in the next section.

Identifying low clouds for aviation application. A naïve Bayesian classifier (e.g., Kossin and Sitkowski 2009) is used to objectively determine the probability of the marginal visual flight rules (Fig. 4c) and instrument flight rules (Fig. 4d) conditions. The GOES-R low cloud base identification algorithm determined the probability that the cloud base (ceiling) is less than 914 m above ground level and the probability that the cloud base is less than 305 m. Both satellite and numerical weather prediction (NWP) model data are used as predictors and ceilometer-based surface observations of cloud ceiling are used to train the classifier. Comparisons are then performed to assess the accuracy of the GOES-R algorithms for detecting ice fog conditions.

PRELIMINARY RESULTS. Radiosonde measurements were only available from Fort Smith, which is about 100 km south of the project site. Vertical profiles of temperature and dewpoint temperature for all of January 2011 at 0000 and 1200 UTC each day are shown in Fig. 5a. These show typical inversion layers below 900–850 mb. This inversion layer usually breaks down when a large-scale frontal system moves in or a subsidence of cold air (Fig. 5c) comes from higher levels. Figure 5b shows RH_w measured at 2 m AGL versus temperature from 1 December 2010 to 31 January 2011 at the Yellowknife International Airport. Available moisture for ice crystal growth (RH_w ~70%) at temperatures <–30°C was much less than available moisture (RH_w ~90%) at temperatures >–10°C, suggesting that ice and snow crystals will likely have a much smaller density at the cold temperatures compared to the warm temperatures. This result is also verified by Miller (1964), who stated that

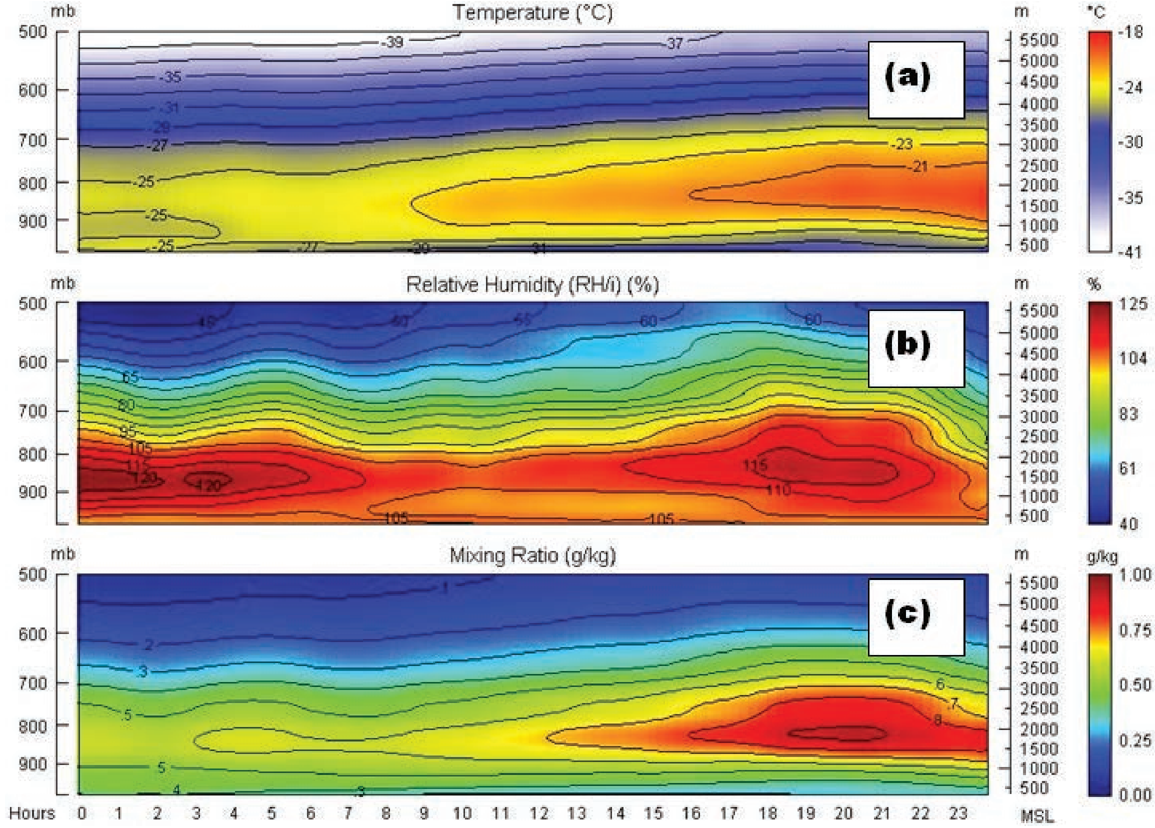

Fig. 3. Time–height cross section of (a) temperature, (b) relative humidity with respect to ice, and (c) vapor mixing ratio measurements from the Radiometrics Profiling Microwave Radiometer during the 17 Jan 2011 ice fog event.

adhesion of snow to surfaces presumably increases as temperature rises toward the freezing point. He also stated that snow loads will be small at low temperatures and moderate to large at temperatures just below freezing. Hobbs (1965), based on the work of Hosler et al. (1957) and Nakaya and Matsumoto (1954), stated that ice crystal adhesion in clouds and fog can decrease by a few dynes at –25°C compared to 700 dynes at 0°C for ice spheres with diameter of 1.0 or 0.15 cm. This shows that snow crystals with very low density (0.2–0.5 g m^{-3}) at cold temperature will have a very low adhesiveness that will result in sweeping out by very low winds (~1 m s^{-1}).

A time–height cross section of radiosonde measurements of temperature and RH_i during 1–31 January 2011 is shown in Fig. 5c. The numbers on the *x* axis represent the number of sounding from day 1 at 0000 UTC (2 times a day). Three ice fog events (16, 17, and 21 January) observed during this time period occurred at temperature <–30°C where RH_i was close to 100%. Note that a cold air mass subsidence is seen above 700 mb and a shallow cold layer with relatively moist air is seen above 900 mb. The warm regions at about –15°C have relatively high mixing ratio (e.g., ~1 g kg^{-1}).

Based on in situ observations at the surface, the occurrence of the ice fog, frost, and light snow is summarized in Table 2. This table shows that ice fog occurred about 14 times (visibility <10 km) during the FRAM-IF project. Light snow conditions were very common during the project, occurring almost every day (including precipitation durations of less than 30 min that are not considered in Table 2). The information on deicing conditions obtained from the First Air flight summaries and present work suggests that ice fog and frost conditions occurred at least 14 and 12 times, respectively. Figures 6a–c are photos

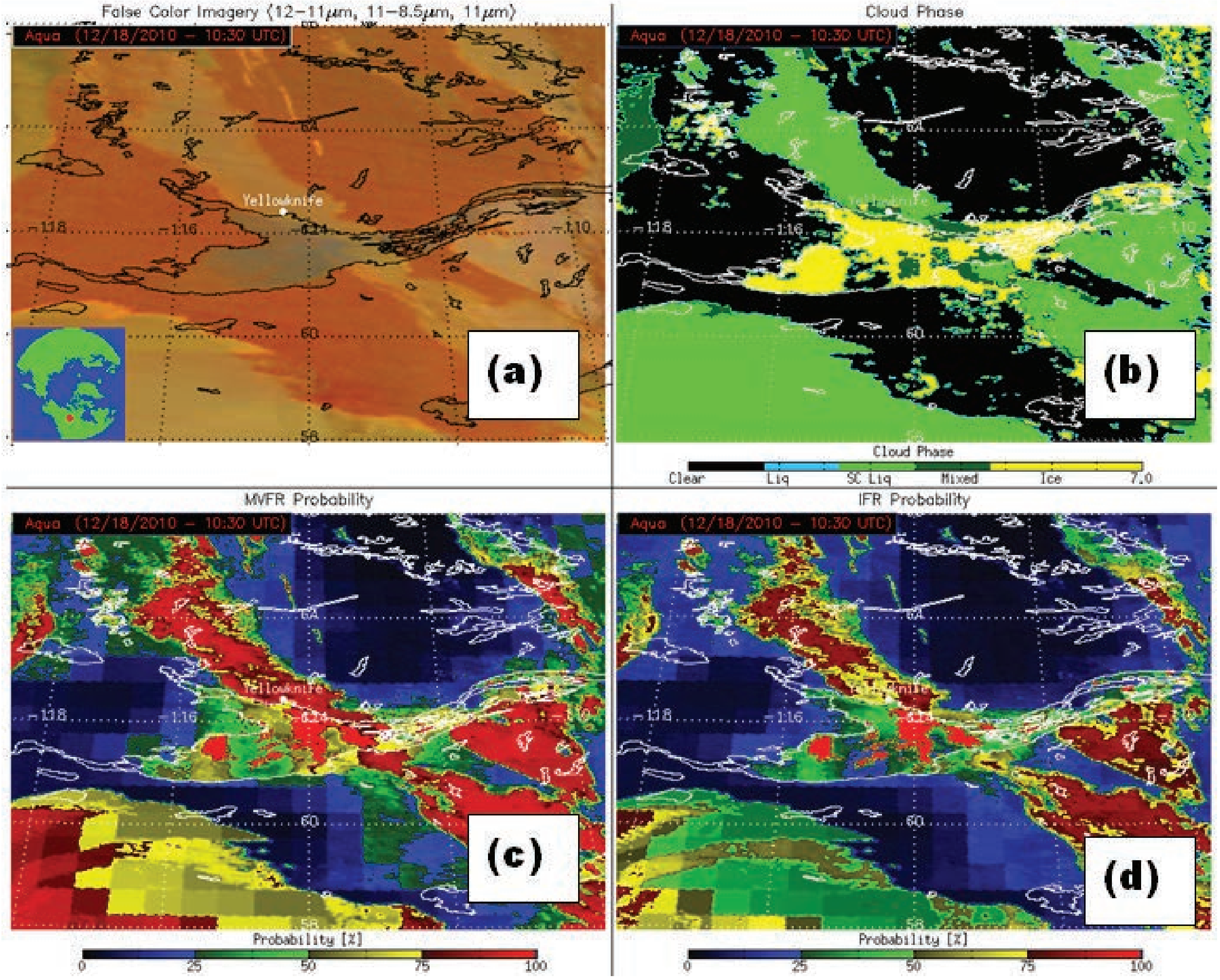

Fig. 4. An *Aqua* MODIS overpass at 1030 UTC 18 Dec 2010 is used to demonstrate cloud phase and low cloud base detection algorithms developed for GOES-R. (a) A false color image. (b) The GOES-R cloud phase product. (c),(d) The GOES-R probability of marginal visual flight rule and probability of instrumented flight rule, respectively.

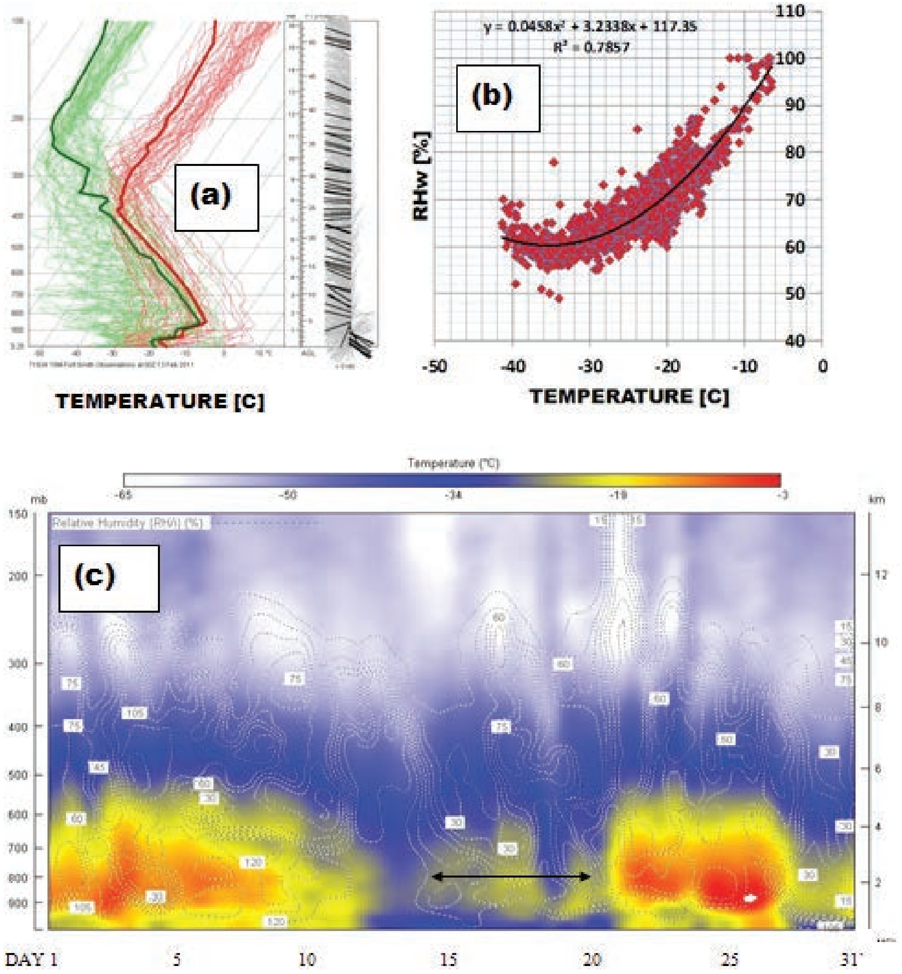

Fig. 5. (a) Temperature (as red lines) and dewpoint temperature (as green lines) profiles from radiosonde measurements for all of January 2011 with thick lines for 0000 UTC 13 Jan 2011; (b) hourly relative humidity with respect to water vs temperature measured at 2 m AGL for Dec 2010 and Jan 2011, with a fit to data; and (c) relative humidity with respect to ice contours overlaid on temperature image for entire January 2011 (2 times per day along the *x* axis); vertical scale is height in km or mb. In (c), the yellow- and red-colored regions approximately indicate ice clouds. The double arrow line shows a time segment for the ice fog events representing infrared cooling conditions during 16, 17, and 21 Jan 2011.

taken during the project at Yellowknife Airport that show frost on the icing sensor, electrical wires, and Vaisala temperature sensor, respectively. Figure 6d shows the heavy frost occurred at −17°C over the Department of Energy, North Slope Alaska site on 10 April 2008 during the FRAM-IF project that was performed as a part of Department of Energy (DOE) Indirect and Semi-Direct Aerosol Campaign (ISDAC) project. The maximum frost thickness reached 2–3 cm over a 12-h ice fog event on 9 April during the period of 9–12 April 2008. If the sensors were not heated, measurements could have been severely compromised.

During the project, measurements showed that there were significant physical differences in frost and snow crystals accumulated on the surfaces. Frost forms on surfaces by the interlocking of vapor molecules at cold temperatures deposited directly from air above (Fig. 6). The Federal Aviation Administration (2012) suggested that holdover times (45 min) for type 1 deicing fluid for frost is 11 to 6 times greater than those (4–8 min) of snow conditions at temperatures < −15°C. This also shows that adhesiveness of the aircraft surfaces for frost is much higher than that of snow. The first author also discussed the issue with deicing operators of the First Air, Inc. in Yellowknife International Airport

Table 2. Summary of significant weather events over 67 days during the FRAM-IF project (24 Nov 2010–31 Jan 2011). Numbers represent any weather event lasting more than about 30 min. Although the integrated occurrence of both ice fog and frost is about 26%, they can also occur at the same time, resulting in slightly lower probability of less than 26%.

Ice fog	Light snow	Heavy snow	Frost	Diamond dust	Clear air	Blowing snow	Ice crystals	Clouds
14	23	8	12	10	13	2	7	8

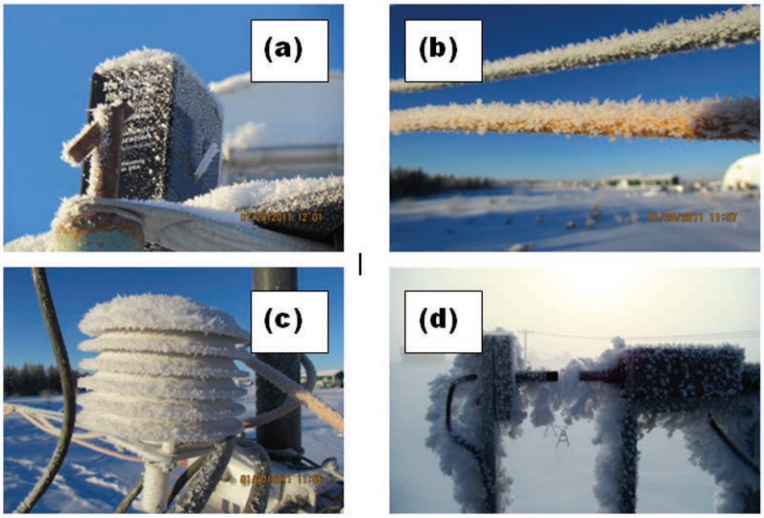

Fig. 6. Ice fog–induced frost on several events: (a) over the Maser icing sensor, (b) over electrical wires, and (c) over the HMP42C sensor on 20 Jan 2011 at –13°C. (d) Heavy frost at –17°C occurred after an ice fog event on the Ice Particle Counter on 10 Apr 2008 during the FRAM-IF project took place at the Department of Energy, North Slope Alaska site.

during the project and they stated that type 1 fluid does not work for temperature < –35°C and they just brush off snow at the aircraft surfaces, but this was not the case with frost conditions.

The dry aerosol spectra time series were measured by the Ultra High-Sensitivity Aerosol Spectrometer that was located in the heated trailer where the temperature was nominally ~15°C. The particles measured were dry as opposed to those measured by the Climatronic Aerosol Profiler (Table 1), which was located out in the ambient environment. During fog-free conditions, the spectra from both sensors indicated a smooth continuation (not shown); however, during ice fog conditions, the Climatronic Aerosol Profiler spectra shifted to the right over larger size ranges (size >0.5 μm), indicating the fraction of aerosols particles growing to ice fog particles.

For larger particle sizes (>10 μm), the Ground Cloud Imaging Probe images and spectral measurements during the project clearly indicated ice fog existence but fog crystal shapes could not be clearly discriminated. The Fog Monitoring Device suggested that their numbers were usually more than 1000 L^{-1}. Overall, ice fog and frost occurred during early mornings following a clear night during periods of high pressure. Winds were usually calm and less than 1 m s^{-1}. These conditions were necessary but not sufficient for ice fog formation on several days. Ice nuclei and availability of moisture were also critical parameters for the ice fog formation and maintenance. Single precipitating (pristine) ice crystals (<500 μm) usually occurred during strong inversion layers with tops at about 1–1.5 km (Fig. 5). Figure 7a for the 16 January case shows that there were many small ice crystals with sizes less than 100 μm. Occasionally, the particles were present at

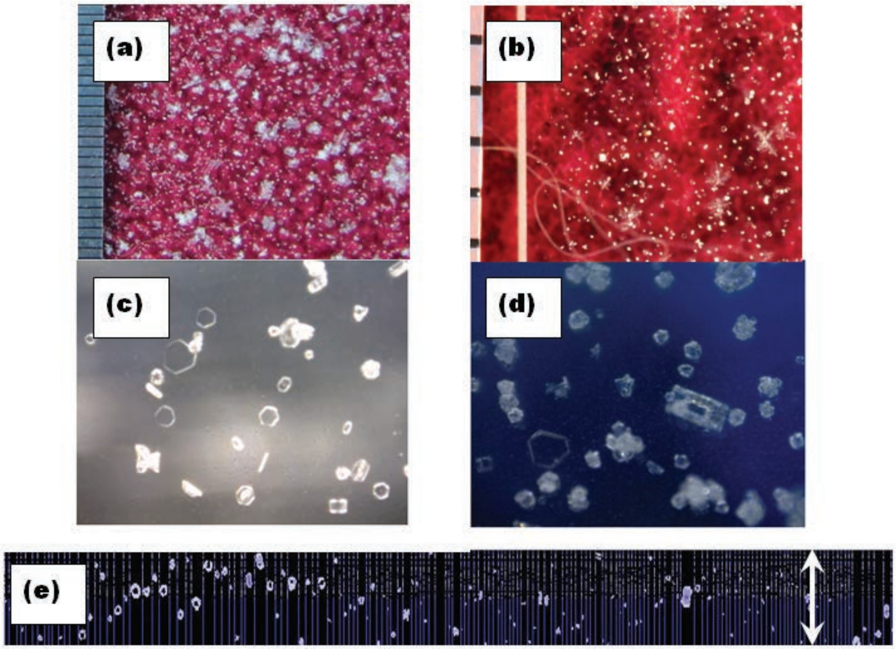

Fig. 7. Ice crystal pictures: (a) small ice crystals and light snow particles (16 Jan 2011), (b) small ice crystals with sizes less than 50 μm (16 Jan 2011), (c) ice crystals with sizes less than 10 μm (18 Jan 2011), and (d) another view of small ice crystals (18 Jan 2011). (e) A ground cloud imaging probe particle image with crystal sizes less than 10 μm and up to 150 μm on 18 Jan 2011.

sizes greater than 1000 μm. These particles were collected over a piece of cloth and their picture taken was with a Canon camera with macro capability. Because of the resolution limitation, small ice particles on the images were seen as spherical. Figure 7b also shows many small ice crystals with sizes <50 μm. Figures 7c and 7d show ice crystal pictures taken with a Barska Microscope at 40 times magnification. The size of these ice crystals at –35°C was about 5–10 μm and their shape was not spherical (opposite of Korolev and Isaac 2003) and they encompassed shapes such as columns, plates, and other varieties. Figure 7e shows that the ice particle images collected on 16 January have sizes <100 μm.

Figure 8 shows the ice crystal imaging sensor (Fig. 8a) and various particle types imaged with the probe (Figs. 8b–d). Figure 8c shows two images of the same ice particle that were taken for ice crystal fall velocity calculation. This technique with increased size resolution may give an estimate of particle fall velocity directly, which could be used to develop a parameterization as function of particle shape that can be used for model applications. Figure 8d shows a stellar ice crystal with maximum dimension of about 1.7 mm taken on 4 January 2011.

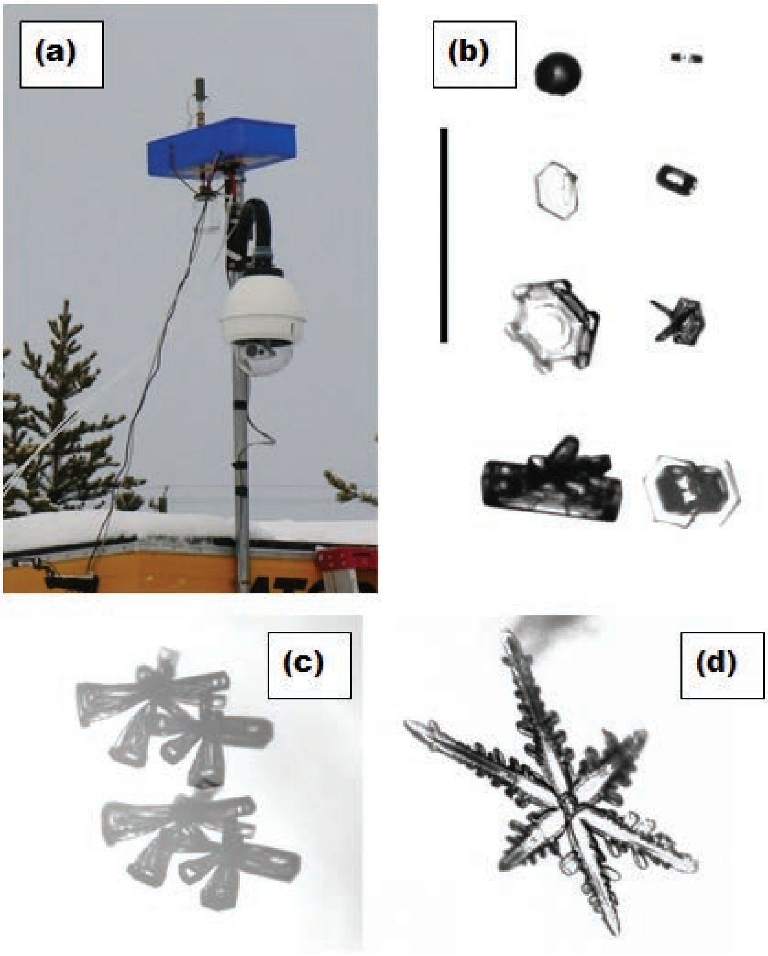

Fig. 8. (a) The ice crystal imaging sensor with its inlet and optical setup are shown at the trailer. (b) A few images taken by Ice Crystal Imaging camera system are shown with a reference scale of 100 mm. Also shown are (c) two images of the same bullet rosette and (d) a rimed stellar ice crystal with six branches.

VISIBILITY AND ITS UNCERTAINTY.

Measurement uncertainty issues related to visibility can be significant when the instruments are not calibrated for low temperatures <–20°C. The FD12P measurements of visibility against its precipitation rate over the entire project are shown in Fig. 9a. The particle shapes are given in the legend. The mean, standard deviation, and 10% and 90% values are also shown in this figure. The light snow, medium snow, and medium ice pellet data points are dominant over three distinct colored shapes as green, black, and blue, respectively. Other data points are randomly distributed. A fit (thicker red line) to snow visibility as a function of precipitation rate and the 10% and 90% lines are also shown on the plot. This shows that for a given precipitation rate, visibility changes were large, possibly implying a less statistical significance in deriving visibility–precipitation rate relationships. The use of precipitation rate for snow visibility estimation in the model simulations can be more accurate than the use of ice water content because its prediction and measurement accuracy is very large compared to precipitation rate. Figure 9b shows visibility versus precipitation rate measurements representing Total Precipitation Sensor (TPS) and FD12P sensors. Visibility is almost constant when Total Precipitation Sensor precipitation rate is greater than 0.5 mm h^{-1}. Both sensors precipitation rates approach each other for large values of precipitation rates. In general, the visibility for each sensor was random when precipitation rate was less than about 0.5 mm h^{-1}.

To assess the visibility uncertainties, visibility from the FD12P (Vis$_{fd}$) and Sentry (Vis$_{se}$) are plotted against each other for an ice fog event (Fig. 10a), a light snow event (Fig. 10b), and the entire dataset (Fig. 10c). During ice fog (Fig. 10c), Vis_{fd} is ~2 times larger than visibility from the Sentry sensor (Vis_{se}) for Vis_{se}>2 km. This ratio decreases with increasing visibility. During light snow (Fig. 10b), Vis_{fd} is substantially less than Vis_{se} for Vis_{se}>8 km. These results may seriously affect the sensor's capability to obtain accurate visibility and need to be further checked for their accuracy. The green line over the data points shown in Fig. 10c represents a visual fit to data and it moves away from the red line (1:1 line) for increasing $\mathrm{Vis}_{se.}$ Usually, Vis_{fd} is ~2 times larger than Vis_{se} (>2 km). In some cases, Vis_{fd} is ~2 times less than Vis_{se} (>2 km). These uncertainties may create a major issue for model validations. Clearly, differences between them are large and significant.

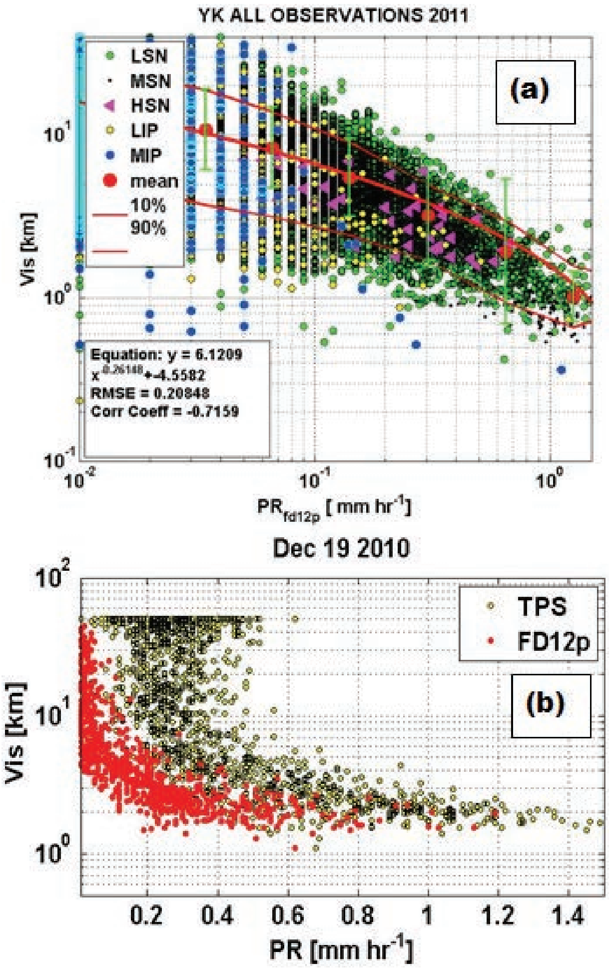

Fig. 9. (a) Visibility vs precipitation rate obtained from FD12P for all data points for the entire project. The particle types are shown on the bar. Mean, 10%, and 90% lines are shown with red lines. The error bars represent standard values (green lines). The equation fitted to mean values is shown on the plot. (b) Visibility vs total precipitation sensor precipitation rate (green) and FD12P precipitation rate (red) for the 19 Dec 2010 case.

ICE FOG PREDICTION.

Global Environmental Multiscale prediction model. Environment Canada currently runs the Global Environmental Multiscale prediction model (Côté et al. 1998) in a limited-area configuration over various domains in Canada with 2.5-km horizontal grid spacing. In this model configuration, clouds and precipitation are predicted by the two-moment version of the Milbrandt and Yau (2005a,b) bulk microphysics parameterization. In this scheme, ice crystals are represented by two categories, with "ice" representing pristine crystals and "snow" representing larger crystals (sizes >250 μm) or aggregates. Each of these particle size distributions is represented by complete gamma functions whose parameters evolve along with the two prognostic variables: the total number concentration and the mass mixing ratio for each particle shape. Currently, the Milbrandt and Yau (2005a,b) algorithm is based on the parameterization of Meyers et al. (1992), which is based on limited aircraft and laboratory measurements and does not represent Arctic conditions. Therefore, the ice fog visibility parameterization developed based on measurements should be used cautiously with the Milbrandt and Yau (2005a,b) scheme. However, the new measurements collected during FRAM-IF will be used to constrain the scheme for the prediction of ice crystal number concentrations, and thus ultimately will improve the prediction of ice fog visibility.

North American Mesoscale Model. For operational applications, National Centers for Environmental Prediction's (NCEP's) 12-km North American Mesoscale Model (Rogers et al. 2009; Ferrier et al. 2002) is used for regular weather guidance over the continental United States. The North American Mesoscale Model[1] is run 4 times per day (0000, 0600, 1200, and 1800 UTC), providing forecast guidance over all of North America with hourly products out to 36 h and 3-hourly outputs at longer ranges at 84 h. The model postprocessor calculates visibility using the extinction as a function of cloud ice water content (Stoelinga and Warner 1999); however, this

---

[1] The 84-h forecasts from the 12-km operational North American Mesoscale Model (NAM) are currently available for 60-h forecasts (at 1.5-km resolution) from the Alaska nest (at 6 km) that includes the Yellowknife area. The NAM runs are being performed for the specific ice fog events over a nested area with 1.5-km resolution.

tends to underestimate the ice fog water content. Since this algorithm may not have been appropriate for ice fog, several alternative methods were tested. The first method uses surface parameters from the model (Zhou and Du 2010), but it only predicts the occurrence of ice fog and not its visibility. The second method includes the effects of moisture advection (Zhou and Ferrier 2008; Zhou 2011), which significantly improved the prediction of ice fog for the 16 January 2010 case. Since ice fog can occur within the boundary layer in conditions not dependent on moisture advection, more research is needed.

Ice fog parameterization. Ice fog can be parameterized assuming that visibility is a function of ice water content and ice crystal number concentration (~1000 L^{-1}) at sizes usually less than 200 μm. In this size range, crystal fall velocity can be about 1 cm s^{-1} depending on its shape. This suggests that ice fog crystals can fall in the air about 36 m over a 1-h time period. This shows that to correctly predict ice fog visibility, model microphysics should be sensitive to low ice water content and high ice crystal number concentrations (Ohtake and Huffman 1969; Gultepe et al. 2008, 2012).

Visibility is strongly related to particle shape, density, ice crystal number concentration, and ice water content. Therefore, the extinction coefficient (β_{ext}) can be obtained as a function of ice crystal number concentration (N_i) and cross-sectional surface area (A_c) of ice crystals. The value of A_c is related to a crystal mass as $m_i = aA_c^b$ (Baker and Lawson 2006), where both a and b are regression coefficients. The β_{ext} obtained from a two-dimensional stereographic optical probe measurements representing low-level Arctic clouds collected during ISDAC (McFarquhar et al. 2011), which took place in the vicinity of Barrow, Alaska, in April of 2008, can be written as a function of both ice water content (IWC) and total N_i (Gultepe et al. 2007). Using a relationship between visibility (Vis) and β_{ext} as Vis = $2.9/\beta_{ext}$ (Gultepe et al. 2009), visibility is then parameterized for ice crystals with size ranges between 10 and 200 μm as

$$Vis = 1.19(IWC \times N_i)^{-0.5066}. \tag{1}$$

If both ice water content and ice crystal number concentration can be known from a forecasting model at each time step, then ice fog visibility can be predicted. The current observations collected during FRAM-IF will allow validation of the visibility estimation from Eq. (1).

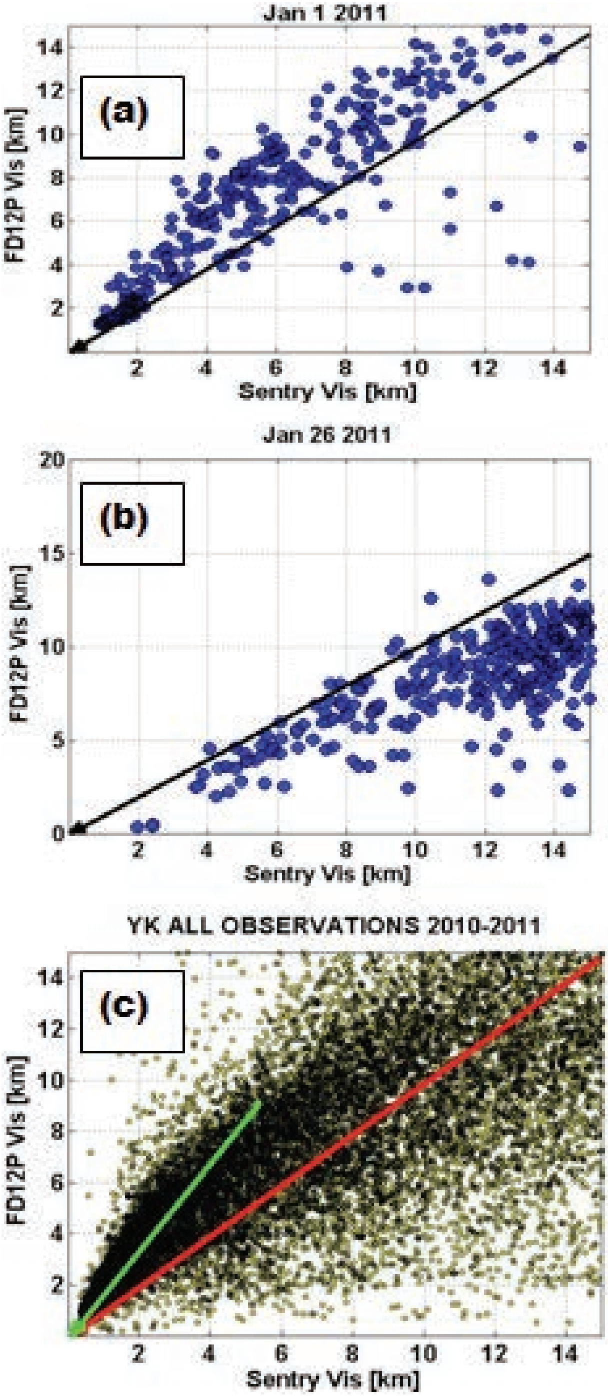

FIG. 10. Visibility comparisons for (a) the ice fog event on 1 Jan 2011 and (b) the light snow event on 26 Jan 2011, where the *y* axis is for FD12P visibility sensor and the *x* axis is for Sentry visibility sensor. (c) Results for the entire project. The red line represents the 1:1 line. The green line is for a visual fit to data for visibility less than 9 km.

Ice fog modeling issues. The current forecasting models were not designed for ice fog and light snow conditions occurring over the Arctic areas. In fact, ice fog occurrence in various space and time scales in a three-dimensional volume can complicate its accurate prediction. The major issues are related to prediction of small ice crystal number concentrations, ice water content, and parameterization of the ice microphysical processes in the cold temperatures. Clearly, deposition nuclei and radiative processes in the clear Arctic boundary layer conditions and existence of an inversion layer need to be predicted accurately for obtaining ice fog visibility and related ice microphysical parameters.

CONCLUSIONS AND FUTURE WORK. Ice fog occurs very often (~14%) in the northern latitudes when temperatures go below −15°C. In fact, ice nuclei can be found at temperatures as high as −8°C (Gultepe et al. 2008). When the temperature is very low, RH_i can easily be saturated with little moisture in the air. Ice fog affects the aviation industry severely by delaying flights and increasing accidents because of low visibilities and increased frost on the planes. When ice fog does occur, it may also lead to increasing frost amount, but frost formation may not always be related to ice fog occurrence. Table 2 suggests that both ice fog and frost usually occur more often than other weather events in the Arctic. Ice fog and frost may also affect power lines, which can lead to disruptions in electrical energy distribution.

Ice fog crystals can be as small as 5–10 μm and usually have sizes less than 200 μm. Depending on their shape and density, they can be suspended in the air for a long time and may generate a very low precipitation rate compared to light snow and snow conditions. They may play an important role in controlling heat loss to the sky in clear air conditions and balancing further cooling dependent on their optical properties. Preliminary conclusions from the FRAM-IF project include the following:

- Ice fog crystal concentrations can be more than 1000 L^{-1}.
- Visibility measurements can be highly variable during the cold temperature below −20°C, especially close to −40°C.
- Particle type from FD12P measurements should be used cautiously and it may only be useful for light, medium, and heavy snow types. Other particle types may not be representative of the real environmental conditions.
- Ice fog can be considered as an ice cloud at the surface. Studying ice fog helps us to better study ice clouds and their microphysical and optical properties.
- Ice fog visibility can be obtained from ice water content and ice crystal number concentration that are prognostically predicted from a forecasting model. Models usually generate ice crystal number concentration less than 100 L^{-1} based on microphysical parameterizations obtained from the aircraft observations; therefore, its prediction becomes questionable and ice crystal number concentration needs to be adjusted for specific environmental conditions.
- Accurate prediction of ice fog visibility, ice water content, and frost conditions can be used advantageously to help plan for the use of aircraft deicing fluids in northern latitudes.
- Visibility–precipitation rate relationships for light snow conditions can be very sensitive to the instrument type. Optical sensors (e.g., FD12P) can be superior against the weighing gauges and hot plate type sensors. Especially during strong wind conditions, measurements from the latter two sensors cannot be accurate for light snow conditions.
- Satellite-based nowcasting of ice fog over Arctic regions could be done if future operational satellites (e.g., the Polar Communication and Weather satellite; Trishchenko and Garand 2011) were launched; current satellites have inadequate space and time resolution in Arctic regions.

Overall, the observations and model simulations will be used to better understand ice fog and frost predictions and their microphysical parameterizations. Detailed analysis of the observations is in progress and the results will be presented in future meetings and publications. It is believed that ice fog studies will provide improved understanding of Arctic and cold cloud systems and visibility forecasts.

ACKNOWLEDGMENTS. Funding for this work was provided by the Canadian National Search and Rescue Secretariat and Environment Canada. ISDAC was supported by the Office of Biological and Environmental Research of the U.S. Department of Energy (Grant DE-FG02-08ER64554) through the Atmospheric Radiation Measurement (ARM) program and the ARM Aerial Vehicle Program with contributions from the Department of Energy Atmospheric Sciences Program, Environment Canada, and the National Research Council of Canada.

REFERENCES

Baker, B., and R. P. Lawson, 2006: Improvement in determination of ice water content from two-dimensional particle imagery. Part I: Image-to-mass relationships. *J. Appl. Meteor. Climatol.,* **45,** 1282–1290.

Benson, C. S., 1965: Ice fog: Low temperature air pollution defined with Fairbanks, Alaska as type locality.

Geophysical Institute (University of Alaska) Rep. UAG R-173, 121 pp.

——, and G. W. Rogers, 1965: Alaskan air pollution—The nature of ice fog and its development and settlement implications. *Proc. 16th AAAS Alaskan Science Conf.*, Juneau, AK, AAAS, 233–245.

Bowling, S. A., T. Ohtake, and C. S. Benson, 1968: Winter pressure systems and ice fog in Fairbanks, Alaska. *J. Appl. Meteor.,* **7,** 961–968.

Calvert, C., and M. J. Pavolonis, 2011: GOES-R Advanced Baseline Imager (ABI) algorithm theoretical basis document for fog and low cloud detection, version 2.0. NOAA/NESDIS, 67 pp.

Côté, J., S. Gravel, A. Méthot, A. Patoine, M. Roch, and A. Staniforth, 1998: The operational CMC-MRB Global Environmental Multiscale (GEM) model. Part I: Design considerations and formulation. *Mon. Wea. Rev.,* **126,** 1373–1395.

Curry, J. A., F. G. Meyers, L. F. Radke, C. A. Brock, and E. E. Ebert, 1990: Occurrence and characteristics of lower tropospheric ice crystals in the Arctic. *Int. J. Climatol.,* **10,** 749–764.

Federal Aviation Administration, 2012: Official FSS holdover time tables. FAA Winter 2012–2013 Notice N 8900, 49 pp.

Ferrier, B. S., Y. Jin, Y. Lin, T. Black, E. Rogers, and G. DiMego, 2002: Implementation of a new grid-scale cloud and precipitation scheme in the NCEP Eta model. Preprints, *15th Conf. on Numerical Weather Prediction,* San Antonio, TX, Amer. Meteor. Soc., 10.1. [Available online at https://ams.confex.com/ams/SLS_WAF_NWP/techprogram/paper_47241.htm.]

Field, P. R., A. J. Heymsfield, and A. Bansemer, 2006: Shattering and particle interarrival times measured by optical array probes in ice clouds. *J. Atmos. Oceanic Technol.,* **23,** 1357–1371.

Girard, E., and J. P. Blanchet, 2001: Microphysical parameterization of Arctic diamond dust, ice fog, and thin stratus for climate models. *J. Atmos. Sci.,* **58,** 1181–1198.

Glickman, T., 2000: *Glossary of Meteorology.* 2nd ed. Amer. Meteor. Soc., 855 pp.

Gotaas, Y., and C. S. Benson, 1965: The effect of suspended ice crystals on radiative cooling. *J. Appl. Meteor.,* **4,** 446–453.

Gultepe, I., and G. A. Isaac, 2002: The effects of air-mass origin on Arctic cloud microphysical parameters during FIRE.ACE. *J. Geophys. Res.,* **107,** doi:10.1029/2000JC000440.

——, ——, and S. G. Cober, 2001: Ice crystal number concentration versus temperature for climate studies. *Int. J. Climatol.,* **21,** 1281–1302.

——, and Coauthors, 2007: Fog research: A review of past achievements and future perspectives. *Pure Appl. Geophys.,* **164,** 1121–1159.

——, P. Minnis, J. Milbrandt, S. G. Cober, L. Nguyen, C. Flynn, and B. Hansen, 2008: The Fog Remote Sensing and Modeling (FRAM) field project: Visibility analysis and remote sensing of fog. *Remote Sensing Applications for Aviation Weather Hazard Detection and Decision Support,* W. F. Feltz and J. J. Murray, Eds., International Society for Optical Engineering (SPIE Proceedings, Vol. 7088), doi:10.1117/12.793281.

——, and Coauthors, 2009: The Fog Remote Sensing and Modeling field project. *Bull. Amer. Meteor. Soc.,* **90,** 341–359.

——, and Coauthors, 2012: Ice fog (pogonip) and frost in Arctic during FRAM-Ice Fog project: Aviation and nowcasting applications. *Proc. 16th Int. Conf. on Clouds and Precipitation,* Leipzig, Germany, ICCP, 13.1.5.

Hobbs, P. V., 1965: The aggregation of ice particles in clouds and fogs at low temperatures. *J. Atmos. Sci.,* **22,** 296–300.

Hosler, C. L., D. J. Jensen, and L. G. Goldshlak, 1957: On the aggregation of small ice crystals to form snow. *J. Meteor.,* **14,** 415–420.

Koenig, L. R., 1971: Numerical modeling of ice deposition. *J. Atmos. Sci.,* **28,** 226–237.

Korolev, A. V., and G. A. Isaac, 2003: Roundness and aspect ratio of particles in ice clouds. *J. Atmos. Sci.,* **60,** 1795–1808.

——, E. F. Emery, J. W. Strapp, S. G. Cober, G. A. Isaac, M. Wasey, and D. Marcotte, 2011: Small ice particles in tropospheric clouds: Fact or artifact? Airborne Icing Instrumentation Evaluation Experiment. *Bull. Amer. Meteor. Soc.,* **92,** 967–973.

Kossin, J. P., and M. Sitkowski, 2009: An objective model for identifying secondary eyewall formation in hurricanes. *Mon. Wea. Rev.,* **137,** 876–892.

Kumai, M., 1964: A study of ice fog and ice-fog splintering nuclei at Fairbanks, Alaska. U.S. Army Cold Regions Research and Engineering Laboratory Research Rep., 150 pp.

Kumar, B., Ed., 2004: *An Illustrated Dictionary of Aviation*. McGraw-Hill, 752 pp.

Lawson, R. P., 2011: Effects of ice particles shattering on optical cloud particle probes. *Atmos. Meas. Tech. Discuss.,* **4,** 939–968.

——, B. A. Baker, P. Zmarzly, D. O'Connor, Q. Mo, J. F. Gayet, and V. Schherbakov, 2006a: Microphysical and optical properties of atmospheric ice crystals at South Pole Station. *J. Appl. Meteor. Climatol.,* **45,** 1505–1524.

——, D. O'Connor, P. Zmarzly, K. Weaver, B. Kaker, Q. Mo, and H. Johnsson, 2006b: The 2D-S (stereo) probe: Design and preliminary tests of a new airborne, high-speed, high-resolution particle imaging probe. *J. Atmos. Oceanic Technol.,* **23,** 1462–1477.

——, E. Jensen, D. Mitchell, B. Baker, Q. Mo, and B. Pilson, 2010: Microphysical and radiative properties of tropical clouds investigated in TC4 and NAMM. *J. Geophys. Res.,* **115,** D00J08, doi:10.1029/2009JD013017.

McFarquhar, G. M, and Coauthors, 2011: Indirect and Semi-Direct Aerosol Campaign. *Bull. Amer. Meteor. Soc.,* **92,** 183–201.

Menzel, W. P., and J. F. W. Purdom, 1994: Introducing GOES-I: The first of a new generation of geostationary operational environmental satellites. *Bull. Amer. Meteor. Soc.,* **75,** 757–781.

Meyers, M. P., P. J. DeMott, and W. R. Cotton, 1992: New primary ice-nucleation parameterizations in an explicit cloud model. *J. Appl. Meteor.,* **31,** 708–721.

Milbrandt, J. A., and M. K. Yau, 2005a: A multimoment bulk microphysics parameterization. Part I: Analysis of the role of the spectral shape parameter. *J. Atmos. Sci.,* **62,** 3051–3064.

——, and ——, 2005b: A multimoment bulk microphysics parameterization. Part II: A proposed three-moment closure and scheme description. *J. Atmos. Sci.,* **62,** 3065–3081.

Miller, D. H., 1964: Interception processes during snowstorms. U.S. Forest Service Research Paper PSW-18, 24 pp.

Nakaya, U., and A. Matsumoto, 1954: Simple experiment showing the existence of liquid water films on the ice surface. *J. Colloid Sci.,* **9,** 41–49.

Ohtake, T., 1967: Alaskan ice fog. *Proc. Internal Conf. on Physics of Snow and Ice,* Part I, Sapporo, Japan, Hokkaido University, 105–118.

——, and P. J. Huffman, 1969: Visual range in ice fog. *J. Appl. Meteor.,* **8,** 499–501.

Pavolonis, M. J., 2010a: Advances in extracting cloud composition information from spaceborne infrared radiances—A robust alternative to brightness temperatures. Part I: Theory. *J. Appl. Meteor. Climatol.,* **49,** 1992–2012.

——, 2010b: GOES-R Advanced Baseline Imager (ABI) algorithm theoretical basis document for cloud type and cloud phase, version 2.0. NOAA, 86 pp.

Petterssen, S., 1940: *Weather Analysis and Forecasting: A Textbook on Synoptic Meteorology.* McGraw-Hill, 505 pp.

Robinson, E., W. C. Thuman, and E. J. Wiggins, 1957: Ice fog as a problem of air pollution in the Arctic. *Arctic,* **10,** 88–104.

Rogers, E., and Coauthors, 2009: The NCEP North American Mesoscale Modeling System: Recent changes and future plans. *Extended Abstracts, 23rd Conf. on Weather Analysis and Forecasting/19th Conf. on Numerical Weather Prediction*, Omaha, NE, Amer. Meteor. Soc., 2A.4. [Available online at https://ams.confex.com/ams/pdfpapers/154114.pdf.]

Schaefer, V. J., and J. A. Day, 1981: *A Field Guide to the Atmosphere.* Houghton Mifflin, 357 pp.

Schmit, T. J., E. M. Prins, A. J. Schreiner, and J. J. Gurka, 2001: Introducing the GOES-M imager. *Natl. Wea. Assoc. Digest,* **25,** 28–37.

——, M. M. Gunshor, W. P. Menzel, J. Li, S. Bachmeier, and J. J. Gurka, 2005: Introducing the next-generation Advanced Baseline Imager (ABI) on GOES-R. *Bull. Amer. Meteor. Soc.,* **86,** 1079–1096.

——, J. Li, J. J. Gurka, M. D. Goldberg, K. J. Schrab, J. Li, and W. F. Feltz, 2008: The GOES-R Advanced Baseline Imager and the continuation of current sounder products. *J. Appl. Meteor.,* **47,** 2696–2711.

Stoelinga, T. G., and T. T. Warner, 1999: Nonhydrostatic, mesobeta-scale model simulations of cloud ceiling and visibility for an East Coast winter precipitation event. *J. Appl. Meteor.,* **38,** 385–404.

Szyrmer, W., and I. Zawadzki, 1997: Biogenic and anthropogenic sources of ice forming-ice nuclei: A review. *Bull. Amer. Meteor. Soc.,* **78,** 209–227.

Thuman, W. C., and E. Robinson, 1954: Studies of Alaskan ice-fog particles. *J. Meteor.,* **11,** 151–156.

Trishchenko, A. P., and L. Garand, 2011: Spatial and temporal sampling of polar regions from two-satellite system on Molniya orbit. *J. Atmos. Oceanic Technol.,* **28,** 977–992.

Wendler, G., 1969: Heat balance studies during an ice fog period in Fairbanks, Alaska. *Mon. Wea. Rev.,* **9,** 512–520.

Wexler, H., 1936: Cooling in the lower atmosphere and the structure of polar continental air. *Mon. Wea. Rev.,* **64,** 122–136.

——, 1941: Observations of nocturnal radiation at Fairbanks, Alaska, and Fargo, North Dakota. *Mon. Wea. Rev.,* **69** (Suppl. 46), 1–21.

Zelenyuk, A., and D. G. Imre, 2005: Single particle laser ablation time-of-flight mass spectrometer: An introduction to SPLAT. *Aerosol Sci. Technol.,* **39,** 554–568.

Zhou, B., 2011: Introduction to a new fog diagnostic scheme. NCEP Office Note 466, 32 pp.

——, and B. S. Ferrier, 2008: Asymptotic analysis of equilibrium in radiation fog. *J. Appl. Meteor. Climatol.,* **47,** 1704–1722.

——, and J. Du, 2010: Fog prediction from a multimodel mesoscale ensemble prediction system. *Wea. Forecasting,* **25,** 303–322.